PCCP

PAPER

Cite this: *Phys. Chem. Chem. Phys.*, 2017, **19**, 30703

Lithium borate $Li_3B_5O_8(OH)_2$ with large second harmonic generation and a high damage threshold in the deep-ultraviolet spectral range†

A. H. Reshak

Received 3rd September 2017,
Accepted 30th October 2017

DOI: 10.1039/c7cp06006h

rsc.li/pccp

The electronic structure and linear and nonlinear optical susceptibility dispersions of lithium borate $Li_3B_5O_8(OH)_2$ are comprehensively investigated. The investigation is achieved on $Li_3B_5O_8(OH)_2$ in the form of single crystals, taking into account the influence of the packing of the structural units on the linear and nonlinear optical susceptibility dispersion. The calculations highlight that the BO_3 structural unit packing is the main source of the large birefringence in $Li_3B_5O_8(OH)_2$ due to the high anisotropic electron distribution, and, hence, it affects the macroscopic second harmonic generation (SHG) coefficients. This work provides a new path for the design of UV-NLO materials with high SHG efficiencies and short cutoff edges by introducing an alkali metal into borates. The large SHG is due to hyperpolarizability formed by co-parallel BO_3 triangle groups. The absorption edge of $Li_3B_5O_8(OH)_2$ occurs at λ = 190 nm and the optical band gap is estimated to be 6.52 eV, which is in good agreement with the experimental data (6.526 eV). The energy gap value confirms that $Li_3B_5O_8(OH)_2$ exhibits an exceptional laser damage threshold and is expected to produce coherent radiation in the deep-ultraviolet (DUV) region. The obtained value of SHG at λ = 1064 nm is about 1.5 times that of the well-known NLO crystal KH_2PO_4 (KDP) at λ = 1064 nm and 3.5 times that of KDP at λ = 190 nm, which is transparent down to the DUV region. Thus, one can conclude that the combination of an alkali metal with borates leads to the generation of promising DUV-NLO crystals. This work is aimed at qualitative and quantitative investigation to report a reliable SHG value and provide details of the NLO tensor for bulk $Li_3B_5O_8(OH)_2$ single crystals.

1. Introduction

The second harmonic generation (SHG) phenomenon is of great interest and has attracted tremendous attention in laser science and technology.[1] Nonlinear optical (NLO) crystals are widely used in optical frequency conversion[2–7] and produce laser radiation at wavelengths that are inaccessible *via* conventional sources.[8–11] In order to produce laser radiation in the ultraviolet (UV) and deep-ultraviolet (DUV) regions, a wide energy band gap is very essential. Therefore, the crystal should exhibit a short absorption cutoff and relatively high birefringence, and the refractive indices dispersion in the UV and DUV regions must be small enough to match the fundamental wave with SHG light.[12] Thus, the designing of efficient and high-performing NLO crystals remains challenging. Borate NLO crystals are among the most promising candidates for this job.[13,14] In borate NLO crystals, B and O atoms form planar triangles $(BO_3)^{3-}$ and $(BO_4)^{5-}$ polyhedra. The BO_3 groups can adopt a coplanar configuration promoting birefringence and SHG. In BO_3 groups, three O atoms are linked with a B atom, eliminating three dangling bonds of the BO_3 groups, which further widens its transparence in the UV and DUV region. Moreover, the highly anisotropic electron distribution in the BO_3 group favors the NLO properties and birefringence,[15] and the large electronegativity difference between B and O atoms is very favorable for transmittance of short-wavelength light.[16] $KBe_2BO_3F_2$ (KBBF) and $Sr_2Be_2B_2O_7$ (SBBO) single crystals[17–19] are very good and promising NLO crystals for generating SHG in the DUV region but due to the high toxicity of the beryllium oxide powders, it remains challenging to safely grow crystals of large size. Therefore, searching for safely grown novel NLO crystals which are able to produce coherent radiation in the UV and DUV regions has attracted the attention of many researchers. Recently, Yang *et al.*[15] substituted Be by Zn to eliminate the toxicity components inherent in the synthesis of KBBF and SBBO from the beryllium oxide powder. Therefore, the discovery of new crystals opens the way to safe crystal growth and increases the efficiency of the SHG to almost double in borate crystals due to the presence of the distorted $(ZnO_4)^{6-}$ tetrahedra. Moreover, the

New Technologies - Research Centre, University of West Bohemia, Univerzitni 8, 306 14 Pilsen, Czech Republic. E-mail: maalidph@yahoo.co.uk; Fax: +420-386 361255; Tel: +420 777729583

† Electronic supplementary information (ESI) available. See DOI: 10.1039/c7cp06006h

introduction of Zn atoms causes a red-shift of the $CsZn_2B_3O_7$ absorption edge to 218 nm.[15] We should emphasize that the unique photochemistry of the borate non-centro-symmetric crystals may be utilized to launch some new photoreaction pathways. Lithium borates have attracted significant interest due to their outstanding properties and structural diversity, and the latter is very impressive due to the fact that boron coordinates with three or four oxygen atoms forming a BO_3 triangle or a BO_4 tetrahedron. The BO_3 triangle or BO_4 unit defines the structure of the borate. Because of the $[BO_3]$ and $[BO_4]$ units, borate crystals are often found to possess hybridized electronic band structures. Lithium borates exhibit piezoelectricity performance,[20] a strong NLO effect[21] and fast ionic conduction.[22] We should emphasize that the presence of lithium in the borate crystals ($Li_3B_5O_8(OH)_2$) makes these crystals efficient NLO crystals in the UV and DUV regions which is attributed to the fact that the alkali-metals do not have the d–d or f–f electronic transitions in the closed d or f orbitals which have an adverse influence on the band gap value. It has been reported that the polar Li-borates, for instance, $Li_3B_5O_8(OH)_2$ or $Li_2B_4O_7$[23,24] are promising materials for nonlinear optical, acoustic, and thermo luminescence applications.[25] Such promising properties have motivated researchers to search for novel acentric or polar compounds in borates with lithium atoms, which are relatively rare.

Due to the excellent properties of alkaline metal borates, the combination of the alkaline metal with borate is expected to produce a new class of novel NLO crystals. Also, it has been reported that the combinations of the alkaline metal borates with wide transparency are prospective materials for efficient NLO properties. It is well known that alkaline metal borates have a perovskite-like structure. The compounds with a perovskite-like structure display interesting structure–property relationships. It has been reported that the introduction of alkali metal atoms can widen the transparency of borates in the ultra-violet region.[26–29] Thus the incorporation of the alkali cations into the borate system could lead to interesting and novel properties. As $Li_3B_5O_8(OH)_2$ crystals possess a perovskite-related structure, it is expected that they exhibit wide transparency which makes them promising candidates for ultra-violet absorption edge materials. These unique properties can make $Li_3B_5O_8(OH)_2$ ideal NLO crystals. It has been reported that $Li_3B_5O_8(OH)_2$ crystals display some very unusual growth features that are absent in many other alkali borates.[30]

Therefore, based on previous experimental work on the synthesis of $Li_3B_5O_8(OH)_2$ single crystals, we use this advantage to investigate the sources of large linear and nonlinear optical properties in $Li_3B_5O_8(OH)_2$ single crystals taking into account the influence of the packing of structural units. It is important to mention that, on the basis of anionic group theory,[31] the overall SHG response of a crystal is the geometrical superposition of the second-order susceptibilities. Therefore, the packing of the BO_3 structural unit may also affect the macroscopic SHG coefficients.[32] The large SHG is due to hyperpolarizability formed by the cations and co-parallel BO_3 triangle groups.[32] Therefore, this work is aimed at qualitative and quantitative investigation to report reliable SHG values and the details of the NLO tensor for $Li_3B_5O_8(OH)_2$ single crystals.

2. Materials and method

2.1. Methodology

In order to gain insight into the microscopic mechanism of the linear and nonlinear optical properties of $Li_3B_5O_8(OH)_2$ single crystals, we performed first-principles calculations using the full-potential method. To perform accurate calculations, the experimental crystallographic data of lithium borate $Li_3B_5O_8(OH)_2$[23,25,30] are optimized utilizing the all-electron full-potential method (wien2k code[33]) within the Perdew–Burke–Ernzerhof generalized gradient approximation (PBE-GGA).[34] The resulting optimized geometrical structure is used to calculate the ground state properties using the recently modified Becke–Johnson potential (mBJ).[35] The crystal structure of lithium borate $Li_3B_5O_8(OH)_2$ is depicted in Fig. 1. For the DFT calculation, the basis functions in the interstitial region are expanded up to $R_{MT} \times K_{max} = 7.0$ and inside the atomic spheres for the wave function. $l_{max} = 10$ and the charge density is Fourier expanded up to $G_{max} = 12$ (a.u.)$^{-1}$. To obtain accurate self-consistency, a mesh of 4500 $\vec{k}$ points in the irreducible Brillouin zone (IBZ) is used. The self-consistent calculations are converged since the total energy of the system is stable within 0.00001 Ry. A mesh of 50 000 $\vec{k}$ points in the IBZ is used to perform the calculation of the linear and NLO properties. The inputs required for calculating the linear and NLO properties are the energy eigenvalues and eigenfunctions which are the natural outputs of band structure calculation. The linear optical properties are calculated using the optical code implemented in the Wien2k package;[33] for more details we refer readers to the users' guide[36] and ref. 37. The formalism for calculating the nonlinear optical properties is given elsewhere.[38–41]

It is well known that the DFT approaches have the ability to accurately predict the ground state properties of the materials, and the developed analytical tools are vital to investigate their intrinsic mechanism. This microscopic understanding has further guided molecular engineering design for new crystals with novel structures and properties. It is anticipated that first-principles material approaches will greatly improve the search efficiency and greatly help experiments to save resources in the exploration of new crystals with good performance.[42–51] For instance, several researchers have used DFT calculations for exploration of the linear and nonlinear optical properties of new NLO materials and have found good agreement with the experimental results. We would like to mention here that, in our previous studies,[52–55] we have calculated the linear and nonlinear optical properties using the FPLAPW method for several systems whose linear and nonlinear optical susceptibility dispersions are known experimentally and very good agreement with the experimental data was obtained. Thus, we believed that our calculations reported in this paper would produce very accurate and reliable results.

2.2. Crystal structure

It has been reported that $Li_3B_5O_8(OH)_2$ crystallizes in the noncentrosymmetric tetragonal space group $P41212$, No. 92 with four formula units per unit cell and unit cell parameters

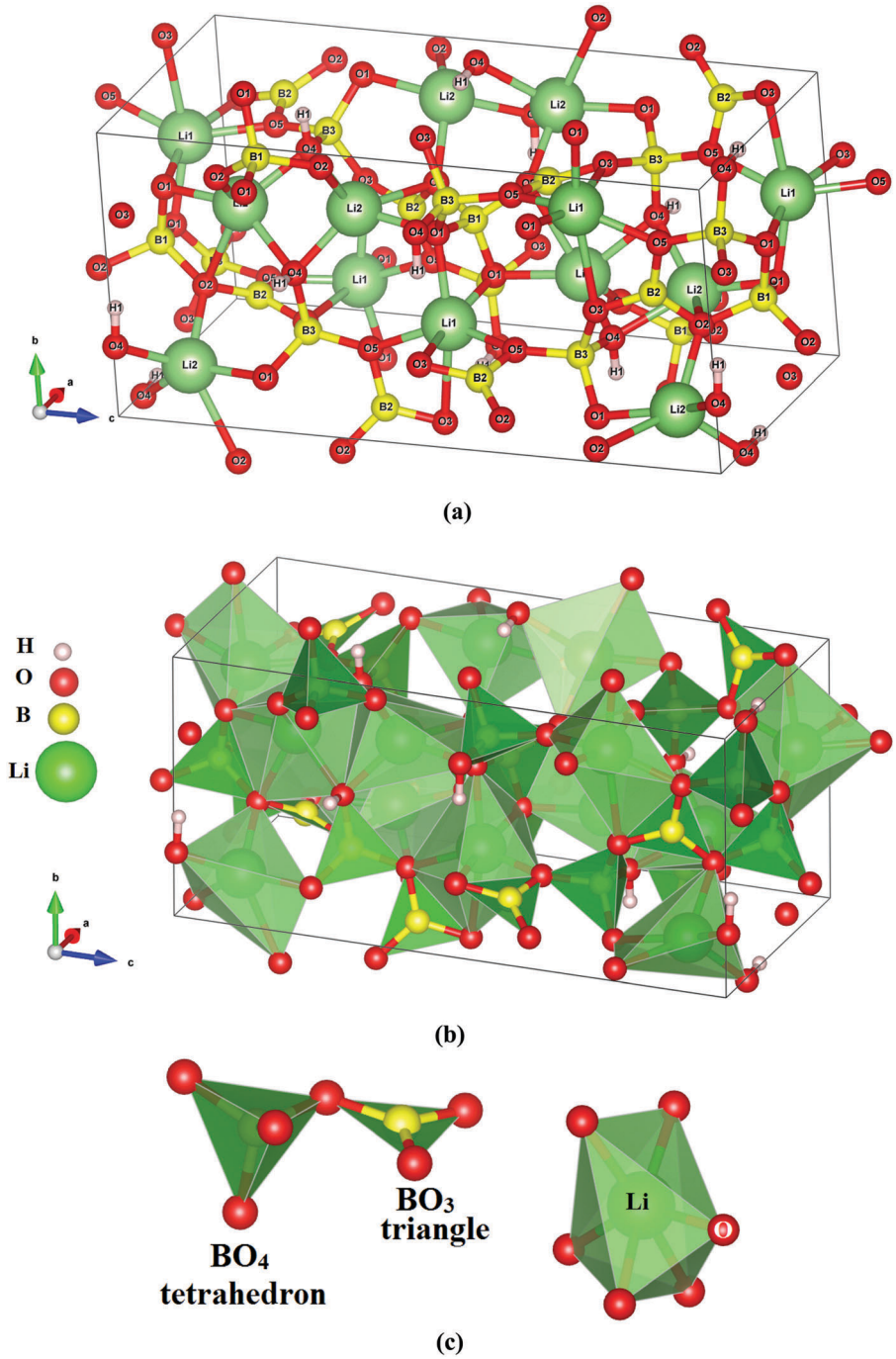

Fig. 1 (a–c) The crystal structure of $Li_3B_5O_8(OH)_2$ which crystallizes in the noncentrosymmetric tetragonal space group *P*41212, No. 92 with four formula units per unit cell. The unit cell consists of two lithium, three boron and five oxygen atoms *i.e.* ten independent atoms. The crystal structure of the tetragonal lithium borate $Li_3B_5O_8(OH)_2$ consists of Li–O polyhedra and the $[B_5O_8(OH)_2]^{3-}$ polyborate anion. The $[B_5O_8(OH)_2]^{3-}$ polyborate anion consists of two 6-membered rings in which two B atoms are surrounded by three O atoms (BO_3 triangle), and the other three B atoms are surrounded by four O atoms (BO_4 tetrahedron). Each 6-membered ring is linked by a common BO_4 tetrahedron and consists of one BO_3 triangle, one BO_3(OH) tetrahedron, and a common BO_4 tetrahedron. The $[B_5O_8(OH)_2]^{3-}$ units are linked together through four exocyclic O atoms to neighboring units and formed a 3-D structure. Moreover, there also exist hydrogen bonds between the framework hydroxyl groups and the exocyclic O atoms. The Li^+ ions are located in the anionic $[B_5O_8(OH)_2]^{3-}$ framework and compensate its negative charge. There are two kinds of coordinated forms for Li^+ ions. Li1 exhibits a 5-fold coordination and coordinates to three O atoms from B–O–B bridges and two O atoms from hydroxyl groups. Li2 exhibits a 6-fold coordination and coordinates to four O atoms from B–O–B bridges and two exocyclic O atoms. The BO_3 triangles adopt a nearly coplanar configuration, which enhances the SHG and the birefringence in borate crystals.

of $a = 6.891\ (4)$ Å, $c = 14.615\ (12)$ Å.[23,25,30] The unit cell consists of two lithium, three boron and five oxygen atoms *i.e.* ten independent atoms[23,25,30] (see Fig. 1). The crystal structure of the tetragonal lithium borate $Li_3B_5O_8(OH)_2$ consists of Li–O polyhedra and the

$[B_5O_8(OH)_2]^{3-}$ polyborate anion. The $[B_5O_8(OH)_2]^{3-}$ polyborate anion consists of two 6-membered rings in which two B atoms are surrounded by three O atoms (BO_3 triangle), and the other three B atoms are surrounded by four O atoms (BO_4 tetrahedron). Each 6-membered ring is linked by a common BO_4 tetrahedron and consists of one BO_3 triangle, one $BO_3(OH)$ tetrahedron, and a common BO_4 tetrahedron. The $[B_5O_8(OH)_2]^{3-}$ units are linked together through four exocyclic O atoms to neighboring units and formed a 3-D structure. Moreover, there also exist hydrogen bonds between the framework hydroxyl groups and the exocyclic O atoms. The Li^+ ions are located in the anionic $[B_5O_8(OH)_2]^{3-}$ framework and compensate its negative charge. There are two kinds of coordinated forms for Li^+ ions. Li1 exhibits a 5-fold coordination and coordinates to three O atoms from B–O–B bridges and two O atoms from hydroxyl groups. Li2 exhibits a 6-fold coordination and coordinates to four O atoms from B–O–B bridges and two exocyclic O atoms.

The experimental crystallographic data[23,25,30] were used as input to perform geometrical relaxation. The experimental lattice parameters were optimized and the experimental atomic positions were relaxed by minimizing the forces acting on each atom; we assume that the structure is totally relaxed when the forces on each atom reach values less than 1 mRy/a.u. The relaxed geometry of $Li_3B_5O_8(OH)_2$ is provided in the ESI.† Geometrical relaxation was achieved by using PBE-GGA. From the relaxed geometry, the electronic band structure was obtained using mBJ. We should emphasize that the mBJ succeeds by a large amount in bringing the calculated energy gap closer to the experimental one. Therefore, the results obtained by mBJ are shown below. Based on the calculated band structure, the complex first-order linear and second-order non-linear optical dispersions are obtained.

3. Obtained results and discussion

The obtained electronic band structure of the tetragonal $Li_3B_5O_8(OH)_2$ crystals reveals the nature of the band gap and

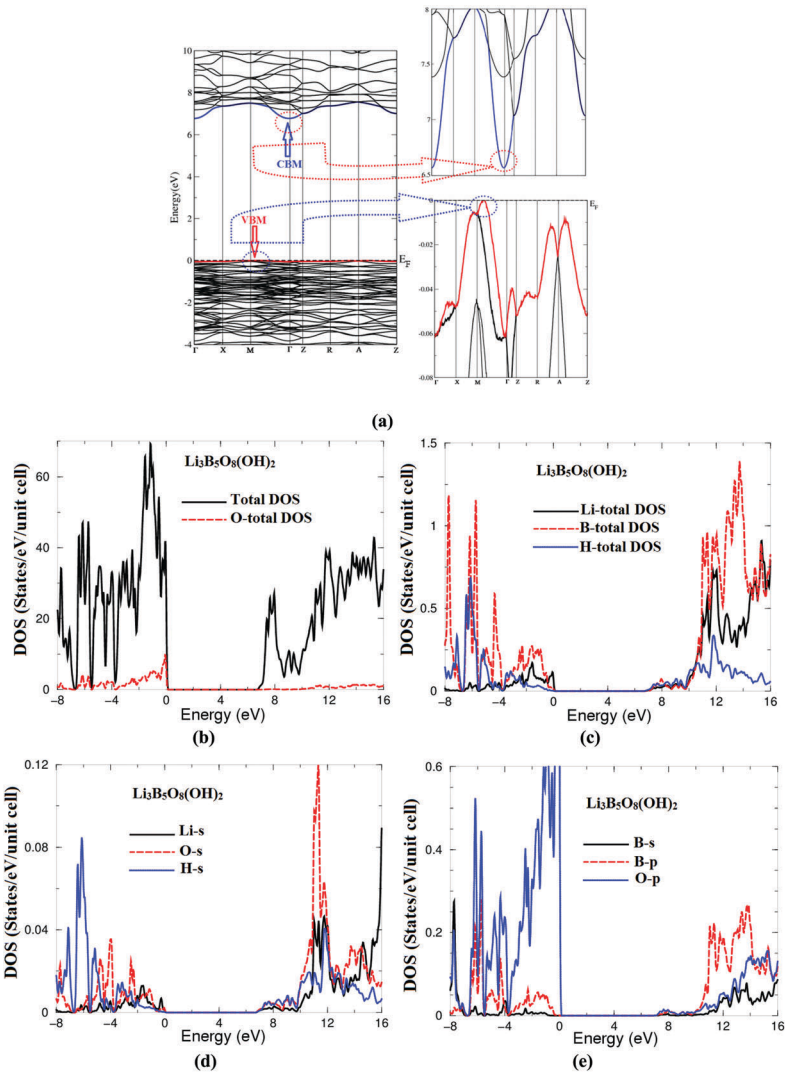

Fig. 2 (a) Calculated electronic band structure of $Li_3B_5O_8(OH)_2$ along with the enlarged bands around the Fermi level *i.e.* the VBM and the CBM; (b–e) the calculated angular momentum projected density of states of $Li_3B_5O_8(OH)_2$.

the high *k*-dispersion bands around the Fermi level (E_F) as shown in Fig. 2a. One can see that the top of the valence band (VBM) is located at the *M* point of the first BZ whereas the bottom of the conduction band (CBM) is situated at *Γ* resulting in a direct band gap. The calculated energy band gap's value using mBJ is estimated to be 6.52 eV in close agreement with the experimental values (6.526 eV).[23,25,30] Therefore, a material with such an energy band gap value is expected to possess a high laser damage threshold.[56,57] It is necessary to highlight that the high *k*-dispersion bands around E_F possess low effective masses and, hence, high mobility carriers, which enhances the charge transfer process. The mobility of the photogenerated carriers significantly influences the SHG efficiency. Moreover, the great effective mass difference (see Table 1) between the electron (e^-) and the hole (h^+) can facilitate the e^- and h^+ migration and separation, and finally improve the SHG performance.

To better understand the relationship between electronic structures and optical properties, the total and the angular momentum projected density of states (PDOS) are computed as shown in Fig. 2b–e. This will help in gaining a detailed description about the orbitals that form the VBM and the CBM and the orbitals which are responsible for the optical transitions according to the dipole selection rules. The obtained PDOS helps in identifying the angular momentum character of the various structures. It was found that the VBM originates mainly from O-2p states with small contribution from Li-2s and O-2s states whereas the CBM is formed by O-2p and B-2p states with small contributions from H-1s, O-2s and Li-2s states. Furthermore, a strong hybridization between Li-2s, O-2s and Li-2s is observed, and also O-2-p states form strong hybridization with B-2s/2p states. The hybridization favors the enhancement of the covalent bonding, and hence, the optical performance due to the fact that covalent bonding is more favorable for the transport of the carriers than the ionic one.[58]

In order to elucidate the characteristics of chemical bonding of $Li_3B_5O_8(OH)_2$, the calculated angular momentum projected density of states was used (Fig. 2b–e). The structure of the valence bands that is confined between −8.0 eV and E_F is mainly formed by O-2s/2p, H-1s, Li-2s and B-2s/2p orbitals. The total number of electrons/electron volts (e/eV) of these orbitals was obtained as follows; O-2p orbital 0.7 e/eV, B-2p orbital 0.28 e/eV, B-2s orbital 0.28 e/eV, Li-2s orbital 0.016 e/eV, O-2s orbital 0.038 e/eV and H-1s orbital 0.082 e/eV. One can conclude that some electrons from O-2s/2p, H-1s, Li-2s and B-2s/2p orbitals were transferred to the VBs and participated in the interactions between the atoms to form covalent bonding. The strength of the covalent bond depends on the degree of hybridization and electro-negativity differences between the atoms. This can be seen directly from the contours of the valence electronic charge density of each atom in $Li_3B_5O_8(OH)_2$.

Table 1 Calculated effective masses

m_e^*/m_o	m_h^*/m_o	$D = m_e^*/m_h^*$	$D = m_h^*/m_e^*$
0.01202	0.01988	0.60462	1.65391

These contours were obtained in different crystallographic planes as shown in Fig. 3. Fig. 3a, shows the (1 0 0) crystallographic plane; it can be seen that the B atom forms strong covalent bonds with the nearest O atoms in BO_3 and BO_4 (see Fig. 3b–d). Due to the electro-negativity differences between B (2.04) and O (3.44) charge transfer occurs towards O atoms as they are surrounded by uniform spheres. It was reported that in borate materials, the large electro-negativity difference between B and O atoms is very favorable for transmittance of short-wavelength light.[59] In general, the B and O atoms in borates form planar triangles $(BO_3)^{3-}$ and $(BO_4)^{5-}$ polyhedra. The BO_3 groups can adopt a coplanar configuration promoting birefringence and SHG. In BO_3 groups, three O atoms are linked with the B atom, eliminating three dangling bonds of the BO_3 groups, which further widens its transparency in the UV and DUV region. Moreover, the high anisotropic electron distribution in the BO_3 group favors the enhancement of the SHG and birefringence.[60] More details can be seen from the (1 0 1) crystallographic plane (Fig. 3b), which reveals that the Li atoms form ionic bonding. Also it shows the $(BO_3)^{3-}$ triangles and $(BO_4)^{5-}$ polyhedra. This supports the finding from the PDOS, which states that there exists strong hybridization between B and O atoms. The strong/weak hybridization may lead to the formation of strong/weak covalent bonding. It is interesting to compare our calculated bond lengths with the measured ones,[23,25,30] as shown in Table 2, which reveals that there is good agreement between the theory and the experiment.

To confirm that the absorption edge of the tetragonal $Li_3B_5O_8(OH)_2$ occurs in the DUV region, the absorption spectra are calculated, as presented in Fig. 4a. The absorption edge's value of the semiconductor materials could be solved as follows; the square of the absorption coefficient $I(\omega)$ is linear with energy (E) for direct optical transitions in the absorption edge region, whereas the square root of $I(\omega)$ is linear with E for indirect optical transitions.[61,62] The data plots of SQRT[$I(\omega)$] and SQ[$I(\omega)$] *versus* E in the absorption edge region are shown in Fig. 4b and c. The left inset of Fig. 4b shows that the SQRT[$I(\omega)$] *vs.* energy deviates from the fitted straight line, whereas SQ[$I(\omega)$] *vs.* E is nearly linear (Fig. 4c). These features suggest that the absorption edge of $Li_3B_5O_8(OH)_2$ caused by direct transitions and the charge transfer from the O-2p orbital at the VBM to the B-2p orbital at the CBM contributes to the absorption edge. Thus, the optical properties of $Li_3B_5O_8(OH)_2$ arise due to the transitions between B-2p and O-2p orbitals with small contributions from Li-2s and H-1s orbitals. Following Fig. 4c, we can conclude that the absorption edge of $Li_3B_5O_8(OH)_2$ occurs at λ = 190 nm and the optical band gap is estimated to be 6.52 eV in good agreement with the experimental data (6.526 eV).[23,25,30]

This observation motivated us to demonstrate the calculated imaginary and real parts of the optical dielectric function (Fig. 4d). The imaginary part shows the first critical points (the absorption edges) for the perpendicular and parallel tensor components along the fundamental crystal axes, which are located at 6.52 eV and the fundamental peaks situated at 8.5 and 12.5 eV. Furthermore, the imaginary part reveals that $\varepsilon_2^{\parallel}(\omega)$

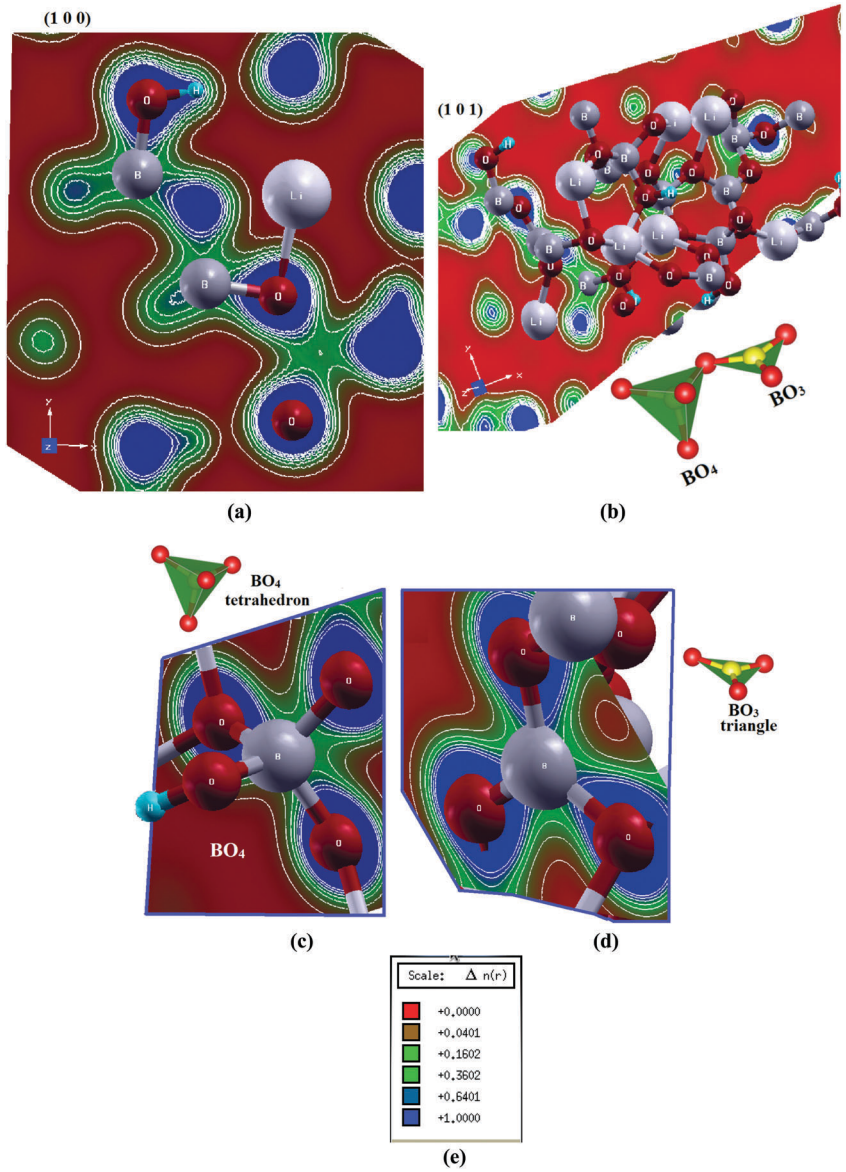

Fig. 3 (a and b) The electron cloud of $Li_3B_5O_8(OH)_2$ in two crystallographic planes namely (100) and (101); (c and d) the electron cloud of the BO_3 anionic groups which exhibit a planar shape with conjugated electron orbitals which make the BO_3 anionic groups the main source of the large birefringence in $Li_3B_5O_8(OH)_2$. The electron cloud of the BO_4 tetrahedron; (e) thermo-scale.

Table 2 Calculated bond lengths in comparison with the experimental data[25b]

Bond	Exp. bond lengths (Å)	Calc. bond lengths (Å)
Li(1)–O(5)	1.962(3)	1.960
Li(1)–O(3)	2.009(3)	2.002
Li(1)–O(2)	2.035(3)	2.033
Li(2)–O(1)	2.0242(15)	2.0239
Li(2)–O(2)	2.056(3)	2.054
Li(2)–O(4)	2.436(3)	2.434
B(1)–O(3)	1.3765(18)	1.3760
B(2)–O(1)	1.4772(18)	1.4769
B(3)–O(2)	1.4636(15)	1.4632
B(3)–O(3)	1.4964(16)	1.4960

is the dominant tensor component at low energies while $\varepsilon_2^{\perp}(\omega)$ acts as the dominant tensor component at high energies, resulting in a considerable anisotropy. The calculated vanishing frequency value (static electronic dielectric constant $\varepsilon_\infty = \varepsilon_1^{\perp}(0)$ and $\varepsilon_\infty = \varepsilon_1^{\parallel}(0)$) of $\varepsilon_1^{\perp}(\omega)$ and $\varepsilon_1^{\parallel}(\omega)$ confirms the occurrence of absorption edges at 6.52 eV, whichcan be explained on the basis of the Penn model $\varepsilon_1(0) \approx 1 + (\hbar\omega_P/E_{\text{optical gap}})$,[2,63] where the calculated $\varepsilon_1(0)$ is inversely related to the energy gap. For $Li_3B_5O_8(OH)_2$ the calculated $\varepsilon_1(0)$ and the plasma energy $\hbar\omega_P$ are given in Table 3. Thus, the $E_{\text{optical gap}}$ is about 6.52 eV and $\lambda = 1239.8/E_{\text{optical gap}} = 190$ nm. Therefore, the calculated $\varepsilon_2^{\perp}(\omega)$, $\varepsilon_2^{\perp}(\omega)$, $\varepsilon_1^{\perp}(\omega)$, $\varepsilon_1^{\parallel}(\omega)$, $\varepsilon_1^{\perp}(0)$ and $\varepsilon_1^{\parallel}(0)$ support our observation that the absorption edge of $Li_3B_5O_8(OH)_2$ occurs at λ = 190 nm and the optical band gap is estimated to be 6.52 eV in good agreement with the experimental data (6.526 eV).[23,25,30] Furthermore, the calculated values of $\varepsilon_1^{\perp}(0)$ and $\varepsilon_1^{\parallel}(0)$ help in

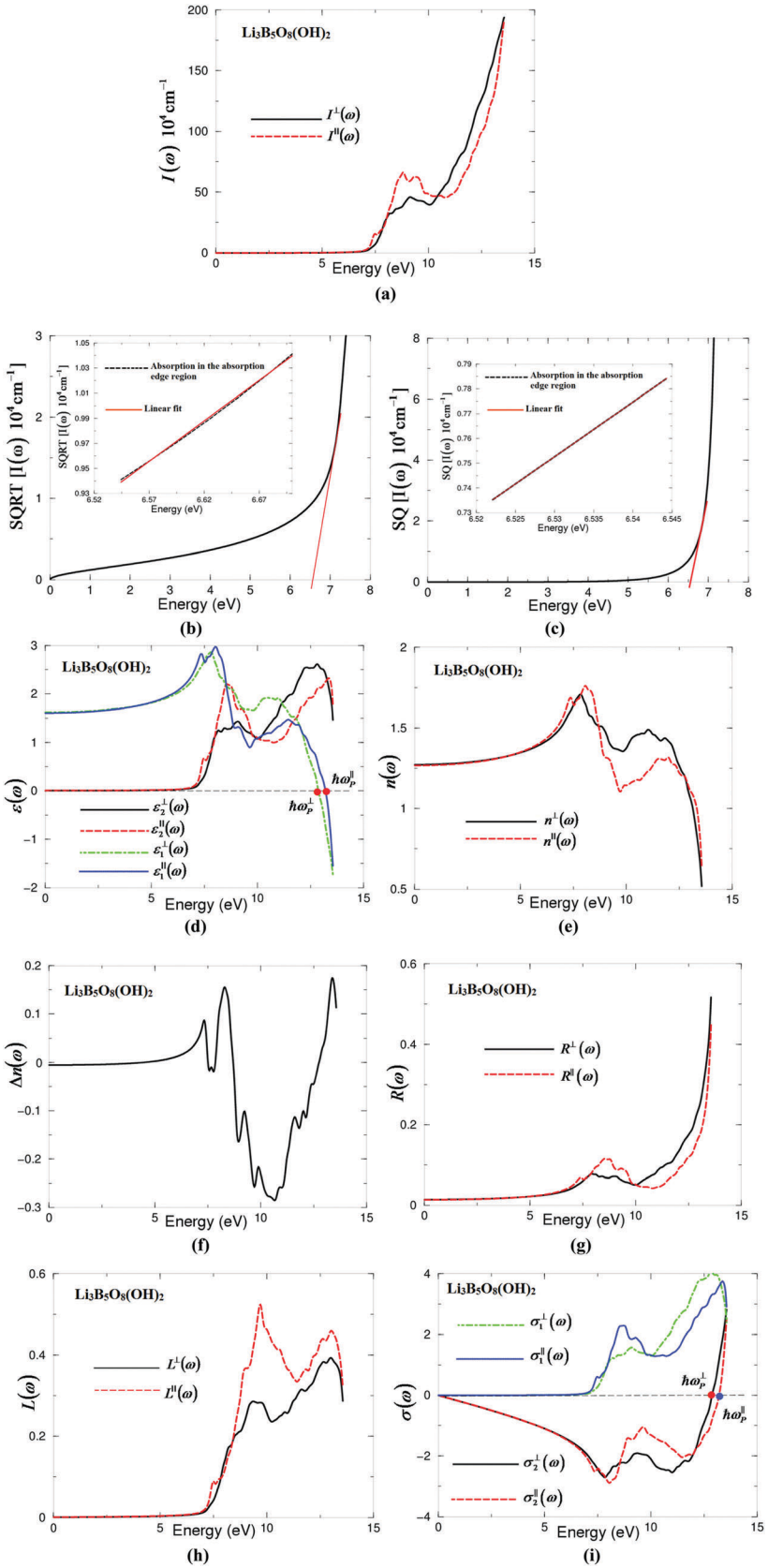
Li3B5O8(OH)2
I(ω) 10⁴cm⁻¹
Energy (eV)
(a)
SQRT [I(ω) 10⁴cm⁻¹]
Absorption in the absorption edge region
Linear fit
(b)
SQ [I(ω) 10⁴cm⁻¹]
(c)
ε(ω)
(d)
n(ω)
(e)
Δn(ω)
(f)
R(ω)
(g)
L(ω)
(h)
σ(ω)
(i)

Fig. 4 (a) The calculated absorption spectra of $Li_3B_5O_8(OH)_2$; (b and c) the data plots of SQRT[$I(\omega)$] and SQ[$I(\omega)$] *versus* E in the absorption edge region are shown in (b) and (c). The left inset of (b) shows that the SQRT[$I(\omega)$] *vs.* energy deviates from the fitted straight line, whereas SQ[$I(\omega)$] *vs.* E is nearly linear. These features suggest that the absorption edge of $Li_3B_5O_8(OH)_2$ caused by indirect transitions and the charge transfer from the O-2p orbital at the VBM to the B-2p orbital at the CBM contributes to the absorption edge. Thus, the optical properties of $Li_3B_5O_8(OH)_2$ arise due to the transitions between B-2p and O-2p orbitals with small contributions from Li-2s and H-1s orbitals. We can conclude that the absorption edge of $Li_3B_5O_8(OH)_2$ occurs at λ = 190 nm and the optical band gap is estimated to be 6.52 eV in good agreement with the experimental data (6.526 eV); (d) calculated $\varepsilon_2^{\perp}(\omega)$ (dark solid curve-black color online) and $\varepsilon_2^{\parallel}(\omega)$ (light dashed curve-red color online) along with calculated $\varepsilon_1^{\perp}(\omega)$ (light dotted dashed curve-green color online) and $\varepsilon_1^{\parallel}(\omega)$ (light dotted curve-blue color online); (e) calculated $n^{\perp}(\omega)$ (dark solid curve-black color online) and $n^{\parallel}(\omega)$ (light dashed curve-red color online); (f) calculated birefringence $\Delta n(\omega)$; (g) calculated $R^{\perp}(\omega)$ (dark solid curve-black color online) and $R^{\parallel}(\omega)$ (light dashed curve-red color online); (h) calculated $L^{\perp}(\omega)$ (dark solid curve-black color online) and $L^{\parallel}(\omega)$ (light dashed curve-red color online); (i) calculated $\sigma_2^{\perp}(\omega)$ (dark solid curve-black color online) and $\sigma_2^{\parallel}(\omega)$ (light dashed curve-red color online) along with calculated $\sigma_1^{\perp}(\omega)$ (light dotted dashed curve-green color online) and $\sigma_1^{\parallel}(\omega)$ (light dotted curve-blue color online).

Table 3 The calculated energy band gap in comparison with the experimental value, $\varepsilon_1^{\perp}(0)$, $\varepsilon_1^{\parallel}(0)$, $\hbar\omega_P^{\perp}$, $\hbar\omega_P^{\parallel}$, $n^{\perp}(\omega)$, $n^{\parallel}(\omega)$, $\Delta n(0)$ and $\Delta n(\omega)$

E_g (eV)	6.52, 6.526[a]
$\varepsilon_1^{\perp}(0)$	1.619
$\varepsilon_1^{\parallel}(0)$	1.606
δ_{ε}	−0.0081
$\hbar\omega_P^{\perp}$	12.884
$\hbar\omega_P^{\parallel}$	13.211
$n^{\perp}(\omega)$	1.272[b], 1.275[c], 1.450[d],
$n^{\parallel}(\omega)$	1.267[b], 1.270[c], 1.473[d],
$\Delta n(\omega)$	−0.005[b], −0.006[c], +0.0141[d]

[a] Ref. 23, 25, 30 (experimental work). [b] Ref. this work at zero limit. [c] Ref. this work at λ = 1064 nm. [d] Ref. this work at λ = 190 nm.

estimating a very important quantity which is called uniaxial anisotropy using the relation $\delta_{\varepsilon} = [(\varepsilon_0^{\parallel} - \varepsilon_0^{\perp})/\varepsilon_0^{\mathrm{tot}}]$.[64] It is found that the uniaxial anisotropy of $Li_3B_5O_8(OH)_2$ is about −0.0081, which confirms the considerable anisotropy. The considerable anisotropy favors an important quantity in SHG and OPO due to better fulfilling of phase-matching conditions determined by birefringence. The birefringence can be obtained from the calculated refractive indices (Fig. 4e) using the expression $\Delta n(\omega) = n_e(\omega) - n_0(\omega)$, see Fig. 4f. The obtained values of the birefringence at the static limit, λ = 1064 nm and at λ = 190 nm are given in Table 3. Birefringence is important in fulfilling the phase-matching conditions. Furthermore, the calculated refractive indices (Fig. 4e) confirm the value of $n(0) = \sqrt{\varepsilon_1(0)}$, Fig. 4e shows that $n^{\mathrm{average}}(0)$ occurs at 1.27 thus $\varepsilon_1^{\mathrm{average}}(0)$ = 1.61, and hence, the absorption edges of $Li_3B_5O_8(OH)_2$ occur at λ = 190 nm. The calculated refractive indices at zero limit, at λ = 190 nm (6.52 eV) and λ = 1064 nm are shown in Table 3 and they are small enough to match the fundamental wave with the SHG light.

To further investigate the linear optical susceptibility dispersion, the reflectivity spectra and the loss function are calculated. The reflectivity spectra (Fig. 4g) show the first minimum at the plasma frequency (*i.e.* 12.5 eV), the energy point where optical spectra of $\varepsilon_1^{\perp}(\omega)$ and $\varepsilon_1^{\parallel}(\omega)$ cross zero, confirming the occurrence of collective plasmon resonance in concordance with our observation in Fig. 4d.

The loss function's peaks (Fig. 4h) are initiated at the values of the plasma frequencies $\omega_P^{\perp}$ and $\omega_P^{\parallel}$ at the energy point where optical spectra of $\varepsilon_1^{\perp}(\omega)$ and $\varepsilon_1^{\parallel}(\omega)$ cross zero. The frequency-dependent optical conductivity (Fig. 4i) can be obtained from the complex first-order linear optical dielectric function following the expression $\varepsilon(\omega) = \varepsilon_1(\omega) + i\varepsilon_2(\omega) = 1 + \frac{4\pi i\sigma(\omega)}{\omega}$.[65,66] It consists of imaginary and real parts; therefore, it completely characterizes the linear optical properties. The imaginary part $\sigma_2^{\perp}(\omega)$ and $\sigma_2^{\parallel}(\omega)$ between 0.0 and the values of $\omega_P^{\perp}$ and $\omega_P^{\parallel}$ exhibit overturned features of $\varepsilon_2^{\perp}(\omega)$ and $\varepsilon_2^{\parallel}(\omega)$, whereas the real parts $\sigma_2^{\perp}(\omega)$ and $\sigma_2^{\parallel}(\omega)$ show similar features to those of $\varepsilon_2^{\perp}(\omega)$ and $\varepsilon_2^{\parallel}(\omega)$. The intersection of the imaginary and real parts of the optical conductivity at zero energy represents the values of $\sigma_2^{\perp}(\omega)$ and $\sigma_2^{\parallel}(\omega)$.

It has been reported that in most borate crystals the SHG responses mainly arise from the coparallel BO_3 triangles, for instance: the KBBF derivatives contain two types of B–O groups and one of the B–O groups consists of coparallel BO_3 triangles. The second B–O group is located between the two adjacent $[Be_2BO_3O_2]$ and connects them together with antiparallel arrangement, resulting in canceling their contribution to the macroscopic SHG response. Hence, the SHG responses in KBBF derivatives mainly arise from the coparallel BO_3 triangles. Therefore, the number density of the coparallel BO_3 triangles will determine the SHG response of the KBBF structures.[53,67] Also in $CsZn_2B_3O_7$, the B_3O_6 groups are located between adjacent $[Zn_2BO_3O_2]$ layers and they are antialigned. Thus, the SHG response of $CsZn_2B_3O_7$ should also come from the coparallel BO_3 triangles, which was confirmed by Yu *et al.*[17] They reported that the net dipole moments of the BO_3 triangles and $(ZnO_4)^{6-}$ tetrahedra are pointed along the polar *c*-axis which means that BO_3 triangles and $(ZnO_4)^{6-}$ tetrahedra contributions to the SHG response are larger than that of B_3O_6 groups.[17] Thus, based on these results and similar to other borates the SHG responses in $Li_3B_5O_8(OH)_2$ mainly arise from the coparallel BO_3 triangles. Therefore, the number density of the coparallel BO_3 triangles will determine the SHG response of the $Li_3B_5O_8(OH)_2$ structure. Our investigation confirms that $Li_3B_5O_8(OH)_2$ possesses large birefringence and considerable anisotropy in the linear optical properties, and the absorption edge occurs at λ = 190 nm. Therefore, based on these promising results, we calculated the nonlinear optical susceptibility dispersion of $Li_3B_5O_8(OH)_2$.

Due to the symmetry, $Li_3B_5O_8(OH)_2$ possesses two non-zero tensor components, these are 132 = −213. The calculated $|\chi_{132}^{(2)}(\omega)| = |\chi_{213}^{(2)}(\omega)|$ are shown in Fig. 5a. The calculated values of these tensor components at the static limit, at λ = 190 nm and at λ = 1064 nm, are presented in Table 4. The calculated value of SHG at λ = 1064 nm is about 1.5 times that of the well known NLO crystal KH_2PO_4 (KDP) at λ = 1064 nm and 3.5 times that of KDP at λ = 190 nm, which is transparent down to the

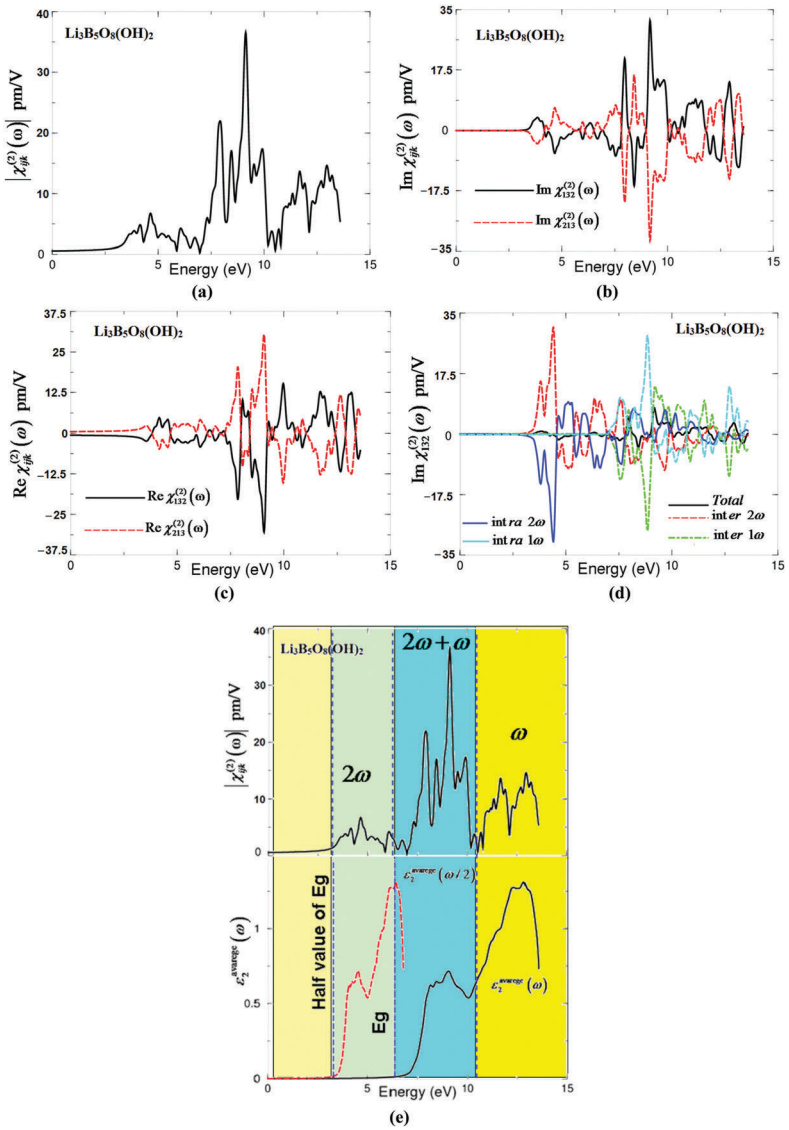

Fig. 5 (a) Calculated $|\chi^{(2)}_{ijk}(\omega)|$ for the five tensor components of $Li_3B_5O_8(OH)_2$; (b) calculated imaginary $\chi^{(2)}_{132}(\omega)$ (dark solid curve-black color online) and $\chi^{(2)}_{213}(\omega)$ (light dashed curve-red color online) spectra; (c) calculated imaginary $\chi^{(2)}_{132}(\omega)$ (dark solid curve-black color online) and $\chi^{(2)}_{213}(\omega)$ (light dashed curve-red color online) spectra; (d) calculated total $\mathrm{Im}\chi^{(2)}_{132}(\omega)$ spectrum (dark solid curve-black color online) along with the intra $(2\omega)/(1\omega)$ (light solid curve-blue color online)/(light dashed doted curve-cyan color online) and inter $(2\omega)/(1\omega)$ (light long dashed curve-red color online)/(light doted curve-green color online) -band contributions; (e) upper panel: calculated $|\chi^{(2)}_{132}(\omega)|$ (dark solid curve-black color online); lower panel: calculated $\varepsilon_2^{xx}(\omega)$ (dark solid curve-black color online); calculated $\varepsilon_2^{xx}(\omega/2)$ (dark dashed curve-red color online).

Table 4 Calculated $|\chi^{(2)}_{ijk}(\omega)|$ and β_{ijk} $Li_3B_5O_8(OH)_2$, in pm/V at the static limit, at λ = 190 nm and at λ = 1064 nm

$Li_3B_5O_8(OH)_2$						
Tensor components	$\chi^{(2)}_{ijk}(0)$	Theory d_{ijk} = 0.5 $\chi^{(2)}_{ijk}(\omega)$ at static limit	$\chi^{(2)}_{ijk}(\omega)$ at λ = 1064 nm	Theory d_{ijk} = 0.5 $\chi^{(2)}_{ijk}(\omega)$ λ = 1064 nm	$\chi^{(2)}_{ijk}(\omega)$ at λ = 190 nm	Theory d_{ijk} = 0.5 $\chi^{(2)}_{ijk}(\omega)$ λ = 190 nm
$\lvert\chi^{(2)}_{132}(\omega)\rvert = \lvert\chi^{(2)}_{213}(\omega)\rvert$	0.7	d_{14} = 0.35	1.28	d_{14} = 0.64	3.00	d_{14} = 1.5
β_{333}	0.413×10^{-30} esu	0.206×10^{-30} esu	0.477×10^{-30} esu	0.238×10^{-30} esu	2.274×10^{-30} esu	1.137×10^{-30} esu

deep-UV region. Thus, one can conclude that the combination of an alkali metal into borates leads to the generation of promising DUV NLO crystals.

Furthermore, we calculated the imaginary and real parts of $\chi^{(2)}_{132}(\omega) = -\chi^{(2)}_{213}(\omega)$, as shown in Fig. 5b and c. It is shown that the 2ω resonance starts oscillating at around 3.26 eV, the half value of the fundamental optical band gap. The highest intensity which is confined between 6.52 and 9.0 eV comes from the contribution of 2ω and ω. The imaginary and real parts are further separated into $2\omega/\omega$ inter-/intra-band contributions.

Fig. 5d shows the $2\omega/\omega$ inter-/intra-band contributions of the imaginary part of $\chi^{(2)}_{132}(\omega)$. It is clear that the $2\omega/\omega$ inter-/intra-band contributions oscillate around zero and exhibit a considerable anisotropy. The sum of those contributions gives the total value of the imaginary part of the SHG.

To have an idea about the origin of the SHG, we have analyzed the spectral features of $|\chi^{(2)}_{132}(\omega)|$. A step forward, the absorptive part of the corresponding dielectric function $\varepsilon_2(\omega)$ as a function of both $\omega/2$ and ω is associated with the spectral structures of $|\chi^{(2)}_{333}(\omega)|$, as shown in Fig. 5e. For simplicity, the spectral structures of $\varepsilon_2(\omega)$, $\varepsilon_2(\omega/2)$ and $|\chi^{(2)}_{132}(\omega)|$ can be divided into three spectral regions. The spectral region confined between $E_g/2$ and E_g is mainly formed by the 2ω resonance, which is associated with the main spectral structure of $\varepsilon_2(\omega/2)$. The second structure between E_g and 11.0 eV is associated with the interference between 2ω and ω resonances, which is associated with the first spectral structure of $\varepsilon_2(\omega)$ and the second structure of $\varepsilon_2(\omega/2)$. It is clear that in this region the ω terms start to oscillate and contribute to the spectral structure of $|\chi^{(2)}_{132}(\omega)|$ in addition to 2ω terms. The third spectral structure from 11.0 eV and 13.5 eV is mainly due to ω resonance which is associated with the second structure in $\varepsilon_2(\omega)$.

Using the obtained value of $\chi^{(2)}_{ijk}(\omega)$, we have obtained the values of the microscopic first hyperpolarizability, β_{ijk},[68] the vector component along the dipole moment direction, at the static limit, at λ = 190 nm and at λ = 1064 nm. We should emphasize that the β_{ijk} term cumulatively yields a bulk observable second order susceptibility term, $\chi^{(2)}_{ijk}(\omega)$, which in turn is responsible for the strong SHG response.[69] In Table 4, we have presented the value of β_{132} at the static limit and at the wavelengths of 190 nm and 1064 nm.

4. Conclusions

A comprehensive *ab initio* calculation was used to investigate the linear and nonlinear optical susceptibility dispersions of $Li_3B_5O_8(OH)_2$ which crystallizes in a non-centrosymmetric tetragonal space group. A bulk structure of $Li_3B_5O_8(OH)_2$ in the form of single crystals is used to investigate the linear and nonlinear optical susceptibility dispersions, taking into account the influence of the packing of structural units on the resulting linear and nonlinear optical susceptibility dispersions. We found that the packing of the BO_3 structural unit is the main source of the large birefringence, and hence, affects the macroscopic SHG coefficients. The large SHG is due to hyperpolarizablity formed by co-parallel BO_3 triangle groups. The accuracy of the mBJ approach shows that the absorption edge of $Li_3B_5O_8(OH)_2$ occurs at λ = 190 nm and the optical band gap is estimated to be 6.52 eV in good agreement with the experimental data (6.526 eV). Therefore, $Li_3B_5O_8(OH)_2$ is expected to produce laser radiation in the DUV region. The resulting SHG is 1.5 times that of the well-known NLO crystal KH_2PO_4 (KDP) at λ = 1064 nm and 3.5 times that of KDP at λ = 190 nm.

Author contribution

A. H. Reshak, as a professor with a PhD in physics and PhD in materials engineering has performed the calculations, analyzed and discussed the results and wrote the manuscript.

Conflicts of interest

The author declares no competing financial interests.

Acknowledgements

The result was developed within the CENTEM project, reg. no. CZ.1.05/2.1.00/03.0088, cofunded by the ERDF as part of the Ministry of Education, Youth and Sports OP RDI programme and, in the follow-up sustainability stage, supported through CENTEM PLUS (LO1402) by financial means from the Ministry of Education, Youth and Sports under the National Sustainability Programme I. Computational resources were provided by MetaCentrum (LM2010005) and CERIT-SC (CZ.1.05/3.2.00/08.0144) infrastructures.

References

1 P. A. Franken, G. Weinreich, C. W. Peters and A. E. Hill, Generation of optical harmonics, *Phys. Rev. Lett.*, 1961, **7**, 118.
2 Y. M. Xu, Y. B. Huang, X. Y. Cui, E. Razzoli, M. Radovic, M. Shi, G. F. Chen, P. Zheng, N. L. Wang and C. L. Zhang, *et al.*, *Nat. Phys.*, 2011, **7**, 198–202.
3 S. Neil, Ultraviolet lasers, *Nat. Photonics*, 2007, **1**, 83–85.
4 D. M. Burland, R. D. Miller and C. A. Walsh, Second-Order Nonlinearity in Poled-Polymer Systems, *Chem. Rev.*, 1994, **94**, 31–75.
5 J. Chiaverini, D. Leibfried, T. Schaetz, M. D. Barrett, R. B. Blakestad, J. Britton, W. M. Itano, J. D. Jost, E. Knill and C. Langer, *et al.*, Nonlinear optics in the extreme ultraviolet, *Nature*, 2004, **432**, 605–608.
6 T. Kiss, F. Kanetaka, T. Yokoya, T. Shimojima, K. Kanai, S. Shin, Y. Onuki, T. Togashi, C. Zhang and C. T. Chen, *et al.*, *Phys. Rev. Lett.*, 2005, **94**, 057001.
7 L. P. Yatsenko, B. W. Shore, T. Halfmann and K. Bergmann, *Phys. Rev. A: At., Mol., Opt. Phys.*, 1999, **94**, R4237.
8 T. Kiss, T. Shimojima, T. Kanaia, T. Yokoya, S. Shin, Y. Onuki, T. Togashi, C. Zhang and C. T. Chen, *J. Electron Spectrosc. Relat. Phenom.*, 2005, **144**, 953–956.
9 J. Meng, G. Liu, W. Zhang, L. Zhao, H. Liu, X. Jia, D. Mu, S. Liu, X. Dong and J. Zhang, *et al.*, *Nature*, 2009, **462**, 335–338.
10 G. Balakrishnan, Y. Hu, S. B. Nielsen and T. G. Spiro, *Appl. Spectrosc.*, 2005, **59**, 776–781.
11 P. Becker, Borate Materials in Nonlinear Optics, *Adv. Mater.*, 1998, **10**, 979–992.
12 X. Jiang, S. Luo, L. Kang, P. Gong, H. Huang, S. Wang, Z. Lin and C. Chen, *ACS Photonics*, 2015, **2**, 1183–1191.

13 H. Huang, L. Liu, S. Jin, W. Yao, Y. Zhang and C. Chen, *J. Am. Chem. Soc.*, 2013, **135**(49), 18319–18322.

14 H. Huang, J. Yao, Z. Lin, X. Wang, R. He, W. Yao, N. Zhai and C. Chen, *Angew. Chem., Int. Ed.*, 2011, **50**, 9141–9144.

15 C. T. Chen, T. Sasaki, R. Li, Y. Wu, Z. Lin, Y. Mori, Z. Hu, J. Wang, G. Aka and M. Yoshimura, *et al.*, *Nonlinear Optical Borate Crystals Principals and Applications*, Wiley-VCH, New York, NY, USA, 2012.

16 Y. Yang, X. Jiang, Z. Lin and Y. Wu, *Crystals*, 2017, **7**, 95, DOI: 10.3390/cryst7040095.

17 H. Yu, H. Wu, S. Pan, Z. Yang, X. Hou, X. Su, Q. Jing, K. R. Poeppelmeier and J. M. Rondinelli, *J. Am. Chem. Soc.*, 2014, **136**, 1264–1267.

18 C. T. Chen, J. H. Lu, T. Togashi, T. Suganuma, T. Sekikawa, S. Watanabe, Z. Y. Xu and J. Y. Wang, *Opt. Lett.*, 2002, **27**, 637.

19 (*a*) B. C. Wu, D. Y. Tang, N. Ye and C. T. Chen, *Opt. Mater.*, 1996, **5**, 105; (*b*) C. T. Chen, G. L. Wang, X. Y. Wang and Z. Y. Xu, *Appl. Phys. B: Lasers Opt.*, 2009, **97**, 9.

20 R. W. Whatmore, N. M. Shorrocks, C. O'hara, F. W. Ainger and I. M. Young, *Electron. Lett.*, 1981, **17**, 11–12.

21 (*a*) H. Konig and R. Hoppe, *Z. Anorg. Allg. Chem.*, 1978, **439**, 71–79; (*b*) S. Lin, Z. Sun, B. Wu and C. Chen, *J. Appl. Phys.*, 1990, **67**, 634–638.

22 K. Byrappa, V. P. Jayantharaia, K. V. K. Shekar, V. Rajeev, V. J. Hanumesh and A. R. Kulkarni, *J. Mater. Sci.*, 1997, **32**, 1599–1602.

23 ICSD database, www.fiz-karlsruhe.de/icsd.html.

24 K. Byrappa and K. V. K. Shekar, *J. Mater. Res.*, 1993, **8**, 864.

25 (*a*) M. Maczka, A. Waskowska, A. Majchrowski, J. Zmija, J. Hanuza, G. A. Peterson and D. A. Keszler, *J. Solid State Chem.*, 2007, **180**, 410–419; (*b*) P. Li and Z.-H. Liu, *J. Chem. Eng. Data*, 2010, **55**, 2682–2686.

26 B. C. Wu, D. Y. Tang, N. Ye and C. T. Chen, *Opt. Mater.*, 1996, **5**, 105.

27 T. Sasaki, Y. Mori, M. Yoshimura, Y. K. Yap and T. Kamimura, *Mater. Sci. Eng.*, 2000, **30**, 1.

28 Y. Mori, Y. K. Yap, T. Kamimura, M. Yoshimura and T. Sasaki, *Opt. Mater.*, 2002, **19**, 1.

29 T. Kanai, T. Kanda, T. Sekikawa, S. Watanabe, T. Togashi, C. T. Chen, C. Q. Zhang, Z. Y. Xu and J. Y. Wang, *J. Opt. Soc. Am. B*, 2004, **21**, 370.

30 K. Byrappa, V. P. Jayantharaja, K. V. K. Shekar, V. Rajeev, V. J. Hanumesh, A. R. Kulkarni and A. B. Kulkarni, *J. Mater. Sci.*, 1997, **32**, 1599–1602.

31 (*a*) N. Ye, Q. Chen, B. C. Wu and C. T. Chen, *J. Appl. Phys.*, 1998, **84**, 555–558; (*b*) C. Chen, N. Ye, J. Lin, J. Jiang, W. R. Zeng and B. C. Wu, *Adv. Mater.*, 1999, **11**, 1071–1078.

32 M. Abudoureheman, L. Wang, X. Zhang, H. Yu, Z. Yang, C. Lei, J. Han and S. Pan, *Inorg. Chem.*, 2015, **54**, 4138–4142.

33 P. Blaha, K. Schwarz, G. K. H. Madsen, D. Kvasnicka and J. Luitz, *WIEN2k, An augmented plane wave plus local orbitals program for calculating crystal properties*, Vienna University of Technology, Austria, 2001.

34 J. P. Perdew, S. Burke and M. Ernzerhof, *Phys. Rev. Lett.*, 1996, **77**, 3865.

35 F. Tran and P. Blaha, *Phys. Rev. Lett.*, 2009, **102**, 226401.

36 http://www.wien2k.at/reg_user/textbooks/usersguide.pdf.

37 C. Ambrosch-Draxl and J. O. Sofo, *Comput. Phys. Commun.*, 2006, **175**, 1–14.

38 S. Sharma, J. K. Dewhurst and C. Ambrosch-Draxl, *Phys. Rev. B: Condens. Matter Mater. Phys.*, 2003, **67**, 165332.

39 A. H. Reshak, PhD thesis, Indian Institute of Technology-Rookee, India, 2005.

40 A. H. Reshak, *J. Chem. Phys.*, 2006, **125**, 03471.

41 A. H. Reshak, *J. Chem. Phys.*, 2006, **124**, 104707.

42 Z. Lin, X. Jiang, L. Kang, P. Gong, S. Luo and M.-H. Lee, *J. Phys. D: Appl. Phys.*, 2014, **47**, 253001.

43 M. I. Kolinko, I. V. Kityk and A. S. Krochuk, *J. Phys. Chem. Solids*, 1992, **53**, 1315–1320.

44 G. E. Davydyuk, O. Y. Khyzhun, A. H. Reshak, H. Kamarudin, G. L. Myronchuk, S. P. Danylchuk, A. O. Fedorchuk, L. V. Piskach, M. Yu. Mozolyuk and O. V. Parasyuk, *Phys. Chem. Chem. Phys.*, 2013, **15**, 6965.

45 A. H. Reshak, Y. M. Kogut, A. O. Fedorchuk, O. V. Zamuruyeva, G. L. Myronchuk, O. V. Parasyuk, H. Kamarudin, S. Auluck, K. L. Plucinskig and J. Bila, *Phys. Chem. Chem. Phys.*, 2013, **15**, 18979.

46 V. V. Atuchin, T. A. Gavrilova, J.-C. Grivel and V. G. Kesler, *Surf. Sci.*, 2008, **602**, 3095–3099.

47 V. V. Atuchin, T. A. Gavrilova, J.-C. Grivel and V. G. Kesler, *J. Phys. D: Appl. Phys.*, 2009, **42**, 035305.

48 O. Y. Khyzhun, V. L. Bekenev, V. V. Atuchin, E. N. Galashov and V. N. Shlegel, *Mater. Chem. Phys.*, 2013, **140**, 558–595.

49 V. V. Atuchin, E. N. Galashov, O. Y. Khyzhun, V. L. Bekenev, L. D. Pokrovsky, Yu. A. Borovlev and V. N. Zhdankov, *J. Solid State Chem.*, 2016, **236**, 24–31.

50 H. Huang, X. Li, J. Wang, F. Dong, P. K. Chu, T. Zhang and Y. Zhang, *ACS Catal.*, 2015, **5**(7), 4094–4103.

51 H. Huang, X. Han, X. Li, S. Wang, P. K. Chu and Y. Zhang, *ACS Appl. Mater. Interfaces*, 2015, **7**, 482–492.

52 A. H. Reshak, *Sci. Rep.*, 2017, **7**, 46415, DOI: 10.1038/srep46415.

53 A. H. Reshak and S. Auluck, *RSC Adv.*, 2017, **7**, 14752.

54 A. H. Reshak and M. G. Brik, *J. Alloys Compd.*, 2016, **675**, 355–363.

55 A. H. Reshak, *J. Appl. Phys.*, 2016, **119**, 105706.

56 J. W. Lekse, M. A. Moreau, K. L. McNerny, J. Yeon, P. S. Halasyamani and J. A. Aitken, *Inorg. Chem.*, 2009, **48**, 7516–7518.

57 J. A. Brant, D. J. Clark, Y. S. Kim, J. I. Jang, J.-H. Zhang and J. A. Aitken, *Chem. Mater.*, 2014, **26**, 3045–3048.

58 F. Wu, H. Z. Song, J. F. Jia and X. Hu, *Prog. Nat. Sci.: Mater. Int.*, 2013, **23**(4), 408–412.

59 Yi Yang, Xingxing Jiang, Zheshuai Lin and Yicheng Wu, *Crystals*, 2017, **7**, 95, DOI: 10.3390/cryst7040095.

60 C. T. Chen, T. Sasaki, R. Li, Y. Wu, Z. Lin, Y. Mori, Z. Hu, J. Wang, G. Aka and M. Yoshimura, *et al.*, *Nonlinear Optical Borate Crystals Principals and Applications*, Wiley-VCH, New York, NY, USA, 2012.

61 H. Huang, Y. He, X. Li, M. Li, C. Zeng, F. Dong, X. Du, T. Zhangd and Y. Zhang, *J. Mater. Chem. A*, 2015, **3**, 24547–24556.

62 H. Huang, Y. He, Z. Lin, L. Kang and Y. Zhang, *J. Phys. Chem. C*, 2013, **117**, 22986–22994.
63 D. R. Penn, *Phys. Rev. B*, 1962, **128**, 2093.
64 G. D. Boyd, H. Kasper and J. H. McFee, *IEEE J. Quantum Electron.*, 1971, **7**, 563.
65 F. Bassani and G. P. Parravicini, *Electronic States and Optical Transitions In Solids*, Pergamon Press Ltd., Oxford, 1975, pp. 149–154.
66 C. Ambrosch-Draxl and J. O. Sofo, *Comput. Phys. Commun.*, 2006, **175**, 1–14.
67 C. T. Chen, Y. B. Wang, B. C. Wu, K. Wu, W. Zeng and L. H. Yu, *Nature*, 1995, **373**, 322.
68 R. Y. Boyd, *Principles of Nonlinear Optics*, Academic Press, NY, 1982, p. 420.
69 R. W. Boyd, *Nonlinear optics*, Academic Press is an imprint of Elsevier, 3rd edn, 2008, ISBN:978-0-12-369470-6.

